1
2
3
4
5
6
7
8
9
10
11
12
13
14 **Larval dispersion along an axially symmetric mid-ocean ridge**
15
16 D.J. McGillicuddy, Jr.[a]
17 J.W. Lavelle[b]
18 A.M. Thurnherr[c]
19 V.K. Kosnyrev[a]
20 L.S. Mullineaux[d]
21
22
24
25
27
28
29
30
31
32
33
34
35 [a]Department of Applied Ocean Physics and Engineering, Woods Hole Oceanographic Institution,
36 Woods Hole, MA 02543, USA. Tel: 508-289-2683 Fax: 508-457-2194 Email:
37 dmcgillicuddy@whoi.edu (Corresponding Author).
38 [b]NOAA/ Pacific Marine Environmental Laboratory, 7600 Sand Point Way, N.E. Seattle, WA,
39 98115, USA. Email: j.william.lavelle@noaa.gov.
40 [c]Lamont-Doherty Earth Observatory, Palisades, NY 10964, USA. Email:
41 ant@ldeo.columbia.edu.
42 [d]Biology Department, Woods Hole Oceanographic Institution, Woods Hole, MA 02543, USA.
43 Email: lmullineaux@whoi.edu.
44
45
46

Abstract

47
48
49   We investigated planktonic larval transport processes along an axially symmetric mid-
50 ocean ridge with characteristics similar to that of the East Pacific Rise (EPR) segment at 9-10°N.
51 The hydrodynamic basis for this study is a primitive equation model implemented in two
52 dimensions (depth and across-ridge), forced at the open boundaries to provide suitably realistic
53 simulation of currents observed on the EPR ridge crest from May to November 1999. Three-
54 dimensional trajectories of numerical larvae are computed assuming homogeneity in currents in
55 the along-ridge direction. Larval dispersal fluctuates significantly in time. Transport distance
56 decreases systematically with height above the bottom where numerical larvae are less subject to
57 strong currents along the flanks of the ridge. The probability that the simulated larvae will be
58 located near the ridge crest at settlement depends strongly on their behavioral characteristics
59 (vertical position in the water column during the larval stage) and the length of their
60 precompetency period.
61
62
63
64 Key words: East Pacific Rise, larval transport, larval behavior, modeling, physical-biological
65 interactions

1. Introduction

For sessile organisms, a life cycle that includes a planktonic stage confers substantial opportunity for dispersal. Hydrodynamic transport of the larval stage is advantageous in terms of colonization of new areas, yet disadvantageous with respect to self-sustenance of local populations. Balance between the conflicting objectives of dispersal and retention is to some degree set by life history parameters (Strathmann, 1985). The maximum time an organism can survive in the planktonic larval stage is referred to as the *larval life span*. The initial time interval after spawning during which a larva is not fit to settle is referred to as the *precompetency period*. From the perspective of larval settlement success, minimization of the precompetency period and maximization of the larval life span provides the most flexibility in terms of dispersal and retention.

Benthic organisms inhabiting hydrothermal vent systems face particularly acute challenges with respect to survival of their planktonic larvae, insofar as areas of suitable substrate are quite limited in spatial extent, relatively few in number, and geographically isolated. Larvae of most hydrothermal vent species are small (Berg and Van Dover, 1987; Mullineaux et al., 1995), and appear to be relatively weak swimmers, suggesting that their dispersal may be determined largely by ocean currents. Planktonic larvae of most dominant vent species do not feed (Lutz et al., 1980; Tyler and Young, 1999). Similar species in shallow water environments have short larval life spans (hours to days). However, physiological studies of Antarctic asteroids have shown that non-feeding larvae may remain viable in the planktonic stage for months, due to lowered metabolism in cold water (Hoegh-Guldberg et al., 1991). The vent tubeworm *Riftia pachyptila* has been cultured to obtain direct estimates of life span (Marsh et al., 2001); the larvae can live on the order of 30-40 days without feeding. If the larvae are transported as passive neutrally-buoyant particles, they have the potential to disperse distances

90   on the order of 100 km in typical East Pacific Rise (EPR) flows (Mullineaux et al., 2002). Using

91   measured currents, inferred larval life spans, and a dispersal model, Chevaldonné et al. (1997)

92   suggested larvae of the vent polychaete *Alvinella* should be able to traverse the distances

93   necessary to migrate between neighboring vent sites along the EPR.

94   Despite limited swimming capabilities during most or all of their planktonic life, larvae

95   may affect their dispersal through behaviors that alter their position above the seafloor. Larvae of

96   species living in shallow water exhibit a variety of behaviors that result in stratification of their

97   populations in the water column (Forward, 1988; Sulkin, 1984; Young and Chia, 1987).

98   Migrations of coastal larvae may occur daily in response to light, tidally in response to salinity or

99   temperature, or ontogenetically (i.e., over the life span of the larva). Ontogenetic migrations

100   typically involve upward floating or swimming during early larval stages (when lipid reserves

101   are replete), maintenance of position during mid stages, and sinking or downward swimming at

102   late stages, when the larva has depleted lipids (and possibly grown a shell) and is ready to settle.

103   This sort of ontogenetic migration appears to enhance retention of larvae in estuarine

104   environments, as different life stages exploit opposing flows in these two-layer systems to

105   minimize net transport from their source region (Dittel and Epifanio, 1990; Thiebaut et al.,

106   1992). In deep water, we do not expect larvae to migrate in response to light, temperature or

107   salinity cues, but we do expect that ontogenetic migrations are possible, given their general

108   prevalence in invertebrate larvae. In this study, we consider two different strategies likely to be

109   exhibited by larvae in deep water: (1) 'passive' (directional swimming and/or buoyancy are

110   either weak or compensating so the larvae are passive tracers within the flow), and (2)

111   'balloonist' (upward movement shortly after fertilization and downward movement shortly

112   before settlement). Balloonist larvae may achieve ontogenetic change in vertical position

4

113   behaviorally, or through changes in buoyancy during larval development. Upward transport of

114   larvae can also be brought about via their entrainment in buoyant plumes of vent fluid (Kim et

115   al., 1994).

116   Our objective herein is to investigate the processes regulating larval dispersal along the

117   EPR. We track a large number of particles subject to fluctuating circulation over an axially-

118   symmetric ridge and examine the sensitivity of larval transport and retention to several life-

119   history parameters, including larval behavior (passive versus balloonist) and length of the

120   precompetency period. An ensemble of simulations spanning a seven-month period of measured

121   currents provides the basis for generating statistics on the time-mean and fluctuating aspects of

122   larval dispersal.

123   We note that our idealized two-dimensional model does not represent along-axis

124   variations in hydrodynamic and ecological characteristics of this environment.   However,

125   several aspects of the EPR lend themselves to two-dimensional approximation. To begin with,

126   ridge topography is to first order symmetric in the across-ridge direction, and roughly

127   homogeneous in the along-ridge direction over distances on the order of 100km. Moreover,

128   analysis of current meter data along the ridge at 9° 10' N, 9° 30' N, and 9° 50' N suggests

129   coherence of velocity in the along-ridge direction (Thurnherr et al., in preparation). Although the

130   present model is far from complete, we view these simulations as a first step toward

131   implementation of spatially-explicit coupled physical-biological models of larval transport in this

132   complex regime, expanding upon earlier models of larval transport that assumed spatially

133   homogeneous currents (Marsh et al., 2001).

134

2. Methods

135

136   Circulation over an idealized 2-d ridge was based on a primitive-equation, baroclinic,

137   hydrostatic, f-plane (latitude = 9.833°N) model described in Lavelle (2006). The model consists

138   of equations for horizontal and vertical velocities, pressure, potential temperature, salinity,

139   density, and turbulent viscosities and diffusivities in both horizontal and vertical directions.

140   Explicit mixing for momentum and other properties was parameterized according to

141   Smagorinsky (1993). Outward propagating baroclinic waves were absorbed at the domain's

142   edge using sponge layers (Lavelle and Thacker, 2008). Invariance of all equations in the along-

143   ridge direction was assumed.

144   Model equations were discretized using finite volume expressions on a rectangular, z-

145   level C-grid (256 x 128 cells), stretched in ridge-orthogonal (x) and vertical (z) directions.   The

146   highest grid resolution (Δx= 440m, Δz = 12.5m) was located at the ridge crest, coarsening to Δx=

147   2.5km and Δz = 50m in the far-field. The solution domain extended upward to the rigid-lid sea

148   surface and to a distance of 150 km both sides of the ridge. Boundary conditions were cyclic in

149   the x-direction and mixed (zero or zero-gradient) in the z-direction. At each time step,

150   discretized equations for momentum and continuity were consolidated into a Helmholtz equation

151   for pressure that was solved using multigrid methods. Momentum equations were leap-frogged

152   in time, with an Asselin filter applied at each time step. Heat and salt equations utilized upstream

153   differencing, suppressing numerical diffusion using the algorithm of Smolarkiewicz and

154   Margolin (1998).

155   Bathymetry (H) was represented by an axially symmetric analytic function:

156    $H = H_{deep} - H_{relief}e^{-\left(\frac{|x-x_0|}{\sigma}\right)}$, where x is distance in the east-west direction, x_0 is the location of the

157   ridge crest, H_{deep} = 3200m, H_{relief} = 700 m, and the e-folding distance σ is 6 km. These

6

158   parameters were estimated by fitting ridge-normal transects of bathymetric data of the 9-10°

159   segment of the EPR described in Wilcock et al. (1993).This *z*-level model represents bathymetry

160   in "stair-step" form; computational artifact due to this discretization was reduced by utilizing the

161   highest spatial resolution (128 vertical cells) practical considering the total time (4782 hrs) and

162   time step (90 sec) of the calculation. Background potential temperature and salinity profiles

163   were taken from the World Ocean Atlas (Conkright et al., 2002), with smoothing applied to

164   property gradients in the upper 250 m.

165   Our approach is to force the model with a time-series of far-field currents, allowing the

166   model interior to adjust dynamically to that forcing. No data are available to provide such

167   forcing directly, so we must rely on inference from existing current measurements near the ridge.

168   Details of this primitive inverse calculation are provided in Appendix A.

169   Currents for the inverse calculation were measured at a depth of 175 m above the axis of

170   the EPR at 9° 50.9' N, 104° 17.6' W during the period May 2 through November 20, 1999. The

171   observations were made with an Aanderaa RCM7 current meter encased in an RCM8 pressure

172   housing for deep ocean use. Basic quality control was carried out by examining the data for

173   anomalous values, but none were found so the entire record was retained. A total of 4872 of

174   these hourly sampled velocity measurements were used to construct the forcing time series.

175   Forcing thus contained frequency components ranging for 0.5 hr^{-1} to 0. 205 · 10^{-3} hr^{-1}. Model

176   currents were spun-up from rest over the ten-day period prior to May 2, 2006, with the forcing

177   ramped up to full amplitude during the first five days.

178   As formulated, the model does not explicitly represent the hydrodynamic effects of the

179   fluid emanating from hydrothermal vents. Motion caused by the buoyancy of vent discharge,

180   even of vent field discharges, will effect regional flow only in a minor way and only locally at

181 horizontal scales that are too small to be resolved by a regional-scale model grid (Lavelle, 1997).

182 Thomson et al. (2003) reported buoyancy-driven convergent horizontal flows of several cm s^{-1} in

183 the deep axial valley of the Endeavour segment of the Juan de Fuca Ridge. Flow of similar origin

184 is not likely to be significant at the EPR, however, because the axial summit trough, where it

185 exists on the EPR, is only a few meters deep (Fornari et al., 1998). Of course, plume dynamics

186 play a primary role in small-scale flows that can retain larvae at their vent of origin (Bailly-

187 Bechet et al., 2008), but our purpose here is to examine the fate of larvae that escape such

188 localized flows and become subject to ambient currents.

189   Lagrangian transport of the numerical larvae was estimated from the hydrodynamic

190 simulations using ensembles of particles released in the flow. Three-dimensional trajectories

191 were computed from the modeled velocities, assuming homogeneity of the velocity field in the

192 along-axis direction. See Werner et al. (1993) and Blanton (1995) for more details on the

193 particle tracking algorithm used in this study. In short, time series of three-dimensional position

194 vectors are computed from modeled velocities using fourth-order Runge-Kutta integration with

195 adaptive stepsize control (Press et al., 1986).

196   In order to bracket a realistic range of larval behaviors, particles were released at 10, 75,

197 125, 175, and 225 meters above bottom (mab) at the ridge crest. The 10mab releases are

198 intended to mimic passive larvae, whereas the releases at 75mab and greater reflect a balloonist

199 strategy whereby larvae rise into the water column either by swimming, buoyancy, or via

200 convection in vent plumes (not explicitly resolved by the model). In either case, the rise time is

201 sufficiently short (hours to days) that horizontal transport during the transit upward constitutes

202 only a small fraction of the total transport during the larval phase.

203   Similarly, the vertical movement during settlement is not explicitly represented. At any

204   time the numerical larvae pass over the ridge crest after their precompetency period, they are

205   assumed to settle to the bottom instantaneously. Clearly, this approach could overestimate

206   settlement insofar as horizontal currents are swift enough to sweep larvae off-axis during the

207   finite time it takes them to descend. However, given the uncertainties in settlement cues and

208   behavioral responses to those cues, we leave the detailed dynamics of the settlement process to

209   future studies.

210   This model does not include the processes by which larvae are recruited into local

211   populations. Moreover, we assume that the ridge crest is uniformly suitable habitat for newly

212   settled larvae. This is clearly not the case in the real ocean, as the organisms of interest require

213   hydrothermal vent environments to survive as adults. Population connectivity between discrete

214   vent communities will be the subject of future work with a fully three-dimensional model. The

215   idealized simulations presented herein constitute a first step in exploring basic patterns of larval

216   transport and dispersion in this complex environment.

217   The larval life span specified for these experiments is thirty days, similar to that

218   measured for the vent tubeworm *Riftia pachyptila* larvae in its non-feeding stage, and

219   representative of larval life span in a variety of invertebrate species. Although larval life spans

220   of several months or longer are possible (Scheltema, 1971), horizontal transport during such

221   extended larval periods would carry larvae well beyond the ridge segment for which the currents

222   simulated herein are representative. The impact of precompetency periods ranging from 5 to 25

223   days is examined via sensitivity analysis. We recognize that mortality can be significant on these

224   time scales, yet we neglect these effects in order to focus our analysis on the physical-biological

225   interactions that control larval transport in this regime.

226

3. Results

3.1 Simulated currents

227

228

229   Using forcing inferred from the current meter data (Appendix A), the model provides a

230   realistic simulation of the observed ridge crest currents (Figure 1). Cross-ridge (zonal) flows are

231   on the order of 10 cm s^{-1}, and subtidal along-ridge (meridional) flows are 4-8 cm s^{-1}. Velocity

232   fluctuations are an order of magnitude larger than the mean flows (Table 1), the latter of which

233   contain only 0.9% of the total kinetic energy. Longer-period oscillations are more prominent in

234   the meridional direction than the zonal direction. Simulated velocities are highly correlated with

235   observations, and the model captures the standard deviations of the observed currents to within

236   5-7%. Root-mean-square differences between simulated and observed velocities are 50% or less

237   of the standard deviation.

238   Currents in the vicinity of the ridge contain significant across-ridge and vertical structure

239   in both their time-mean and fluctuating components (Figures 2, 3). Strongest currents occur

240   along the flanks of the ridge, with a time-mean of ca. 5 cm s^{-1} directed poleward on the western

241   flank and equatorward on the eastern flank (Figure 2B). These meridional jets span ca. 600m in

242   the vertical, from 2400m to 3000m depth, and extend ca. 10km in the zonal direction. Transport

243   in the two jets averages 0.19 and -0.34 Sv over the course of the seven month simulation. The

244   simulated jets are associated with significant perturbations to the density field (Figure 2), owing

245   to the fact they are in approximate geostrophic balance. Specifically, isopycnals tend to dome

246   upward above the ridge and plunge downward along the flanks of the ridge. A time-averaged

247   high-resolution hydrographic cross-section at the EPR 9°N site is qualitatively consistent with

248   these isopycnal deflections (Thurnherr et al., in preparation).

10

249   Extensive validation of the simulated jets is not possible due to a paucity of direct

250   measurements of these currents. Nonetheless, available observations are generally consistent

251   with the model results. For example, a time-mean velocity profile derived from a moored

252   profiler located 10km west of the ridge axis at 9° 30' N confirms the existence of the flank flow

253   predicted by the model (Figure 4). Although the magnitude of the observed current falls within

254   the envelope of simulated mean profiles between the crest and 15km off-axis, the vertical extent

255   of velocity maximum is broader in the model than in the observations. The fact that the velocity

256   profile observations come from a time period different from the current meter record used to

257   force the model suggests the flank currents are a persistent feature of the mean circulation of the

258   ridge system. This result was confirmed by performing an additional hydrodynamic simulation

259   in which the model forcing was derived from a velocity record 128 mab at the ridge crest

260   contemporaneous with the off-axis current meter presented in Figure 4. Long-term mean flows

261   and their variability were very similar to those presented in Figures 1-4.

262   Additional evidence for northward flow west of the ridge comes from a tracer release

263   experiment at the EPR 9-10° ridge segment in November-December 2006 (Jackson et al., in

264   press). Direct inference of the flow speed is not possible because the time interval over which

265   the tracer resided in the jet (as opposed to ambient waters) is not known. A small part of the

266   tracer moved from 9° 30' to 9° 50' in 33 days, suggesting a minimum meridional velocity along

267   the flank of 1 to 2 cm s^{-1} (Jim Ledwell, personal communication).

268   A transect of velocity observations from a Lowered Acoustic Doppler Current Profiler

269   (LADCP) during the same study detected residual flows northward to the west of the ridge and

270   southward to the east of the ridge, as in the model result (Thurnherr et al., in preparation).

271   Similarly sheared mean flow is present in other regimes, such as the Juan de Fuca Ridge at 45°N

272   (Cannon and Pashinski, 1997), suggesting this phenomenology may be a common characteristic

273   of mid-ocean ridge systems.   Essential to the formation of these topographically trapped flows

274   are the Earth's local vertical rotation rate and advective nonlinearities. Details of the flow

275   patterns depend on the topography of the ridge, local stratification, and the ambient currents.

276   Long-term mean flows in the zonal and vertical directions are weaker and confined to the

277   region close to and above the crest (Figure 2 A,C). However, shorter-term zonal mean flows

278   over the EPR are not as weak as those depicted here; monthly mean zonal flows calculated from

279   the current meter data vary between -1.2 to +1.2 cm s^{-1}. What this serendipitously low seven-

280   month mean flow period reveals is a weak recirculation cell above the ridge crest. Divergence of

281   the zonal flow at crest depth and convergence several hundred meters above leads to downward

282   vertical flow in a thin column above the crest and a broader upward flow in the adjacent waters.

283   This pattern is reminiscent of the circulation that maintains the so-called "cold dome" above

284   seamounts (Brink, 1995; Lavelle, 2006). Unfortunately there are no reliable measurements of

285   vertical velocity above the ridge crest, so the realism of the simulated downwelling cell cannot

286   be assessed directly.

287   In contrast to the ridge crest where standard deviations in velocity are much larger than

288   the mean, standard deviations of the ridge flank currents are approximately the same magnitude

289   as the mean flows (Figure 2). Further insight into the nature of this variability is provided by

290   time-series of velocity components across the ridge at the depth of the crest (Figure 3). The

291   location and spatial extent of the ridge flank jets fluctuate in time, with their far edges sometimes

292   extending to nearly 20 km off axis (Figure 3B). Poleward and equatorward transports are

293   generally not balanced. On a few occasions sub-tidal meridional flow on both sides of the ridge

294   has the same direction. However, most of the time the two jets flow in opposite directions, with

295   the interface between them moving back and forth across the ridge crest ($x=0$). Cross-ridge

296   displacement of the interface is also expressed in the zonal and vertical velocity components

297   (Figure 3 A,C): eastward flow coincides with upwelling on the western flank and downwelling

298   on the eastern flank, whereas westward flow coincides with downwelling on the western flank

299   and upwelling on the eastern flank. An important consequence of this back-and-forth sweeping

300   of the ridge current system is that velocities at the ridge crest are periodically impacted by both

301   jets, enhancing the subtidal frequency components of the flow in the meridional direction relative

302   to those in the zonal flow—a characteristic clearly evident in the current meter record (Figure 1).

303

304   *3.2 Lagrangian visualization of the flow patterns*

305   To illustrate some key characteristics of the transport patterns, passive particles were

306   released instantaneously along a cross-ridge transect and tracked during an example one-month

307   time period (Figure 5). Particle displacements are relatively modest amongst those released at

308   225m above the depth of the ridge crest, with lagrangian trajectories spanning approximately

309   100m in the vertical and 40km in the along-ridge direction.   Vertical and along-ridge

310   displacements increase dramatically with depth, such that trajectories of the particles released at

311   10m above the depth of the ridge crest span 500m in the vertical and 150km in the along-ridge

312   direction. Particles released above the flanks of the ridge are particularly prone to large

313   displacements as they become entrained into current jets along the ridge (Figures 2,3). Episodic

314   reversals in the cross-ridge flow can transport particles from one side of the ridge up and over the

315   crest and back down the other side of the ridge. This tendency is best visualized in animated

316   presentations of these results, available in the "cross_section_release" subdirectory of the

317   supplemental documentation[1].

318   Because these trajectories are derived from an example one-month time period of the

319   simulation, they do not precisely mimic the mean properties of the flow depicted in Figure 2.

320   Nevertheless, some aspects of the mean flows are evident, such as the tendency for particles in

321   the ridge flank currents to be transported poleward on the west flank of the ridge and

322   equatorward on the east flank (most visible in particles released 10mab and 125mab). Further

323   aloft, the flow during this time period is predominantly southward, a result that is also apparent

324   in trajectories of particles released continuously at the ridge crest (Figure 6; see section 3.3

325   below).

326   *3.3 Dispersal of simulated larvae with a 30-day life span*

327   Larval dispersal patterns were simulated by releasing particles at the ridge crest every 12

328   minutes at depths of 10, 75, 125, 175, and 225 mab in the flow simulated from May to November

329   1999. Each particle was tracked for a larval life span of 30 days.   Animated presentations of

330   particle trajectories for September-October are available in the "time_dependent_release"

331   subdirectory of the supplemental documentation[2]. With this large ensemble of particles (total

332   108,000) for the period May to November, it is possible to compute probability density functions

333   (pdfs) of larval dispersal patterns as a function of time and space (Figure 6).   Monthly

334   distributions of trajectory endpoints indicate that the numerical larvae can travel up to hundreds

335   of km in the along-axis direction, but their net displacement in the cross-axis direction does not

336   exceed ±20 km during their thirty-day life span. Patterns of dispersal vary significantly in time.

337   In June-July and August-September cases, maximum dispersal distances were up to 200 km to

[1] Also available at http://science.whoi.edu/users/mcgillic/papers/epr2d/movies/cross_section_release/
[2] Also available at http://science.whoi.edu/users/mcgillic/papers/epr2d/movies/time_dependent_release/

338   the south of the release point (a distance that exceeds the total length of the 9-10°N ridge

339   segment). In June-July, almost 50% of the total number of particles exceeded 100 km

340   displacement, with a bimodal distribution (one to the NNW and the other to the SSE).

341   Dispersion is also highly sensitive to vertical positioning. Particles farther off the bottom

342   traveled shorter distances and had a higher probability of resupply to the ridge crest.

343   Overall settlement rates of the simulated larvae, calculated as the fraction of particles in

344   the water column directly above the ridge crest at the end of the 30-day larval life span, ranges

345   from <1% to nearly 5% (Figure 7). As stated in the Methods section, these estimates assume

346   instantaneous movement of the larvae from the water column to the bottom, neglecting

347   potentially important details of the settlement process. For example, a balloonist larva overlying

348   the ridge crest at the end of its larval life span could be swept away from suitable habitat in the

349   finite time required to reach the bottom. Similarly, a larva just off-axis could be transported

350   toward favorable habitat during descent. Explicit modeling of the settlement process, including

351   behavioral response to environmental cues, is an important avenue for future research.

352   Simulated settlement systematically increases with height off the bottom of the initial

353   release points, such that particles released 225mab are approximately three times more likely to

354   be located over the ridge crest at the end of the larval life span (Figure 7). Temporal variations

355   in settlement are substantial, with more than fivefold differences amongst the bi-monthly bins.

356   These variations reflect time-dependence in dispersal, which fluctuates with the hydrodynamic

357   regime during each bi-monthly period (Figure 6). For example, the dramatic decline in

358   settlement in June-July resulted from shearing of the larval distributions into two distinct peaks

359   located NNW and SSE of the ridge crest, such that a very small proportion of the larvae resided

360   above favorable habitat at the end of the larval period.

361   Despite these dramatic temporal variations, it is still meaningful to compute time-mean

362   pdfs of larval dispersal for the seven month simulation (Figure 8, top row). The northwest-to-

363   southeast orientation of the pdfs results from the tendency for mean flow to the north on the

364   western flank of the ridge, and southward flow on the eastern flank of the ridge (Figure 2B).

365   Decreasing dispersal distance with height above bottom reflects less vigorous currents aloft.

366

367   *3.4 Influence of precompetency and cued settlement on dispersal*

368   The preceding results are based on an assumption that precompetency period is the same

369   as the larval life span. If the larvae have a precompetency period shorter than their life span,

370   there is a longer time interval over which settlement can occur. If they have the ability to sense

371   favorable habitat and settle on that cue, retention along the ridge can increase dramatically

372   (Figure 8, rows 2-4). Overall, the degree of retention is highly sensitive to the period of

373   precompetency (Figure 9). Even a modest decrease in precompetency period from the larval life

374   span improves the odds of settlement by an order of magnitude or more: for particles released

375   10mab, retention increases from less than 1% for a 30 day precompetency period (Figure 7) to

376   ca. 15% for a 25 day precompetency period (Figure 9). This large increase in the proportion of

377   larvae that settle successfully on the ridge reflects the fact that larvae with a precompetency

378   period shorter than the life span benefit from a longer time interval over which settlement can

379   occur (Jackson and Strathmann, 1981). Consequently, their exposure to suitable habitat is

380   increased by the vigorous cross-ridge displacements induced by the time-varying flow (Figures

381   1-3,5). These cross-ridge displacements decrease with height off the bottom, and as such the

382   increase in retention due to decreasing the precompetency period is diminished, albeit still a

383   factor of ten: for particles released 225mab, retention increases from less than 3% for a 30 day

16

384   precompetency period (Figure 7) to ca. 30% for a 25 day precompetency period (Figure 9). The

385   trend of increasing retention with shortening precompetency is consistent throughout the range of

386   parameter space examined herein, such that retention for a 5 day precompetency period varies

387   from 50% (10mab) to 75% (225mab). For all depths, increasing the period of competency

388   increases settlement along the ridge and decreases the number of larvae lost from the system

389   (Figures 8,9). Of course, these results are likely to depend on the assumptions that the simulated

390   larvae have a perfect ability to sense suitable habitat below, and settle immediately on that cue.

391   Again, more explicit representation of the settlement process would help shed light on these

392   sensitivities.

393

394   **4. Discussion**

395   The complex system of currents simulated in this axially-symmetric representation of the

396   EPR influences planktonic larval dispersal in a number of ways. To begin with, along-ridge

397   transport is sensitive to vertical position. During a thirty-day life span, passive larvae released

398   10mab spanned ±200km in the along-ridge direction. In contrast, maximal transport distances

399   for balloonist larvae released 225mab were only about half that of their passive counterparts.

400   Garcia Berdeal et al. (2005) noted a similar trend of decreasing dispersal with height above

401   bottom in an analysis of ADCP current meter data from the Juan de Fuca Ridge, although those

402   observations came from within an axial valley—a very different topographic setting than the

403   EPR. The opposite trend (increasing dispersal with height above bottom) was inferred by

404   Mullineaux et al. (2005) based on velocity profiles at the Juan de Fuca Ridge from Thomson et

405   al. (1990) and Cannon and Pashinski (1997). Part of this discrepancy may be due to small-scale

406   topographic effects on the currents measured near bottom at Juan de Fuca that are not resolved in

407   our model. However, observations at the EPR between 9-10°N reveal currents directly over the

408   crest tend to decrease with depth (Thurnherr et al., in preparation), similar to the profiles used in

409   the Mullineaux et al. (2005) analysis. Thus it seems that small-scale topographic effects are not

410   the root of the apparent discrepancy. A more likely explanation is the along-flank flow, which is

411   more vigorous at crest depth than further up in the water column (Fig.2B). Our inference that

412   dispersal distances increase with depth, even though the horizontal velocities directly above the

413   crest decrease with depth, is directly related to the presence of spatial variability in the velocity

414   field. Such spatial variability is not accounted for in dispersal estimates derived from single

415   current-meter records.

416   Vertical position in the water column affects not only transport distance, but also delivery

417   of larvae to suitable habitat. Our simulations demonstrate that for the cases in which the

418   precompetency period is the same as the larval life span, vertical position of the initial release

419   points accounts for nearly threefold variations in time-mean settlement of larvae at the ridge

420   crest. Whereas time-mean settlement was ca. 1% for particles released 10mab, settlement of

421   particles released 225mab was almost 3% (Figure 7).

422   Both dispersal and settlement vary significantly in time, owing to the fluctuating

423   hydrodynamic environment characteristic of the EPR. Depending on flow conditions, net

424   transport of larvae can occur in either direction along the ridge, with substantial variations in

425   transport distance. Mean flows oriented to the north on the western flank of the ridge and to the

426   south on the eastern flank of the ridge tend to orient larval distributions in the northwest-

427   southeast directions, although the manifestations of such shear dispersion are highly time-

428   dependent. Monthly mean settlement of larvae varies by an order of magnitude for the cases in

429   which the precompetency period is the same as the larval life span.

430   Based on these results, it appears that the balloonist strategy of rising well above the

431   ridge crest improves the odds for local retention of larvae, insofar such behavior tends to isolate

432   them from the vigorous near-bottom currents that are present along the ridge flanks. All other

433   physical and biological factors being equal, species with a balloonist larval stage can presumably

434   achieve a self-sustaining population with lower fecundity than those with a passive larval stage.

435   In contrast, species with passive larvae would have an advantage with respect to colonizing a

436   new area, by virtue of the longer dispersal distances associated with transport in strong near-

437   bottom currents.

438   Evidence for both long-distance colonization and local retention has been described at the

439   EPR. Mullineaux et al. (in preparation) describe drastic changes in species composition at the

440   EPR subsequent to a catastrophic eruption during which all extant communities were destroyed.

441   Of the new colonists detected after the eruption, one species had never been found on that ridge

442   segment before, suggesting import of larvae from distant sources. On the other hand, Adams and

443   Mullineaux (2008) detected correlations between larval supply and currents at the EPR that

444   could be explained by local sources of larvae. Metaxas (2004) interpreted relative spatial

445   homogeneity in planktonic larval abundance and flux at scales of 2km and less at several vent

446   sites in the northeast Pacific to suggest local retention. Local retention may also be facilitated by

447   topographic confinement and circulation within deep rift valleys, such as is present at the

448   Endeavour segment of the Juan de Fuca ridge (Thomson et al., 2003). However, given the

449   strength of the currents observed in ridge systems, local retention would require a precompetency

450   period of no longer than a day or two.

451   Our results are different from an earlier study (Marsh et al., 2001) of larval dispersal on

452   the EPR 9-10°N ridge segment.   Marsh et al.'s computations indicate that at the end of the 26

453   day life span, the along-axis distribution of surviving larvae peaked at the along-axis location of

454   their release (x=0 in their Figure 4c). More than 80% of the surviving larvae were located within

455   ±60km of the release site, and the distribution was skewed to the south. The maximum along-

456   axis dispersal distance was 103km to the south. In contrast to the unimodal distribution

457   predicted by Marsh et al., the along-axis distribution predicted herein is bimodal (Figure 10).

458   Only 50% of the larvae are located within 60km of the release site, and peaks of the distribution

459   reside at 50km to the north and 100km to the south of the release site. Locations of these peaks

460   are near the maximum distances present in the Marsh et al. distribution, and the tails of the

461   distribution predicted herein surpass their dispersal distances by fifty percent to the south, and a

462   factor of three to the north.

463   Why are the results of the present study different than those of Marsh et al.? Although

464   the two investigations were couched in the same study site, our methods differ in both biological

465   and physical aspects. First, the larval life span used herein (30 days) was slightly longer than

466   that used by Marsh et al. to compute their along-axis distribution of survivors (26 days). Second,

467   Marsh et al. assumed 100% mortality of larvae transported beyond 25km of the ridge crest,

468   whereas the present simulations did not include any mortality except that which occurs if a

469   numerical larva is located off-axis at the end of its life span. Although Marsh et al. assumed all

470   larvae within 25km of the ridge crest to be "survivors," our settlement computations (Figures

471   7,9) include only those larvae that are located directly above the ridge crest at the time of

472   settlement. Thus the along-axis distribution of larvae presented in Figure 10 reflects the pre-

473   settlement condition (cf. 175mab panel in the top row of Figure 8) in order to be as comparable

474   as possible to the Marsh et al. result.

475   Notwithstanding these differences in the biological assumptions used in estimating larval

476   dispersal, the primary reason for the differences in the results of the two studies is the

477   hydrodynamic basis of the transport computations. Whereas Marsh et al. used horizontal

478   velocities observed at the ridge crest and assumed spatial uniformity in currents, the present

479   study fit velocity observations with a hydrodynamic model to infer a dynamically consistent

480   velocity field. Spatial structure in the velocity field (Figures 2-5) underlies a key facet of our

481   results, as the bimodal nature of the time-mean along-axis distribution (Figures 8,10) is a direct

482   consequence of mean southward flow on the eastern flank of the ridge and mean northward flow

483   on the western flank of the ridge. Moreover, the presence of a vertical component to the motion

484   of the larvae simulated herein provides them exposure to the more swift along-ridge flows during

485   times when they are subject to cross-ridge displacement, resulting in greater along-axis transport

486   overall.

487   It is important to note that the Marsh et al. study used a current meter record from a

488   different time period (December 1999 to April 2000) than that used herein (May to November

489   1999). In comparing the two records, Marsh et al. found that the later time series yielded longer

490   dispersal distances than the earlier record used in the present study. Therefore, were the

491   comparison between these two approaches to be carried out using the same current meter record,

492   the differences in dispersal would likely be even larger.

493

494   **5. Conclusions**

495   Although the physical model used herein is idealized, it provides a hydrodynamic

496   environment that is significantly more complex than spatially uniform models used in some prior

497   studies of larval transport in deep-ocean ridge systems. Energetic sheared flow along the ridge

498   flanks significantly increases dispersion of passive larvae near the bottom, transporting them

499   much farther and in more complex spatial patterns than a spatially uniform model based on ridge

500   crest currents would predict.   Of course, there remain a number of additional physical and

501   biological complexities that must be grappled with in future studies. To begin with, a fully three-

502   dimensional model will be required to implement a realistic bathymetric setting that can

503   accommodate along-axis variations in the hydrodynamic environment. Such models will also

504   facilitate explicit representation of discrete vent communities, permitting detailed analysis of

505   their interconnectivity from a larval perspective. Several biological aspects are also in need of

506   additional study, including mortality during the larval stage, the specific behaviors by which

507   newly spawned larvae ascend into the water column, as well as their responses to environmental

508   cues for descent and subsequent settlement.

509   Models such as these could eventually be useful for predicting aspects of larval supply to,

510   and colonization of, newly-opened vents. In hydrodynamic systems similar to the EPR, when a

511   new vent opens far from other active vents (e.g., > 100 km) one might expect the initial colonists

512   to be species that disperse predominantly in the strong, near-bottom currents. In contrast, initial

513   colonists at a new vent opening in the neighborhood of other established vents (tens of km away)

514   might be dominated by balloonist species. Near-bottom dispersers with very short

515   precompetency periods also would be potential early colonists of neighboring new vents. At

516   present, our understanding of vertical larval positioning behaviors in vent species is limited, but

517   vertical sampling in the field (expanding on efforts by Mullineaux et al. 2005 and others) should

518   help us determine which species are dispersing at what heights above bottom. That information,

519   in combination with inferences on precompetency period, should enable species-level predictions

520   of initial colonists at new vents.

521

Appendix A: Inverse calculation for model forcing

A primitive inverse calculation is used to derive forcing that causes the model to mimic

current meter observations above the ridge crest. Let the currents over the ridge over the time

period [0,T] at measurement interval dt be represented in rotary spectral form (e.g. Emery and

Thomson, 1998) where temporal cyclicity of the currents is assumed:

$$\left(u(t)+iv(t)\right)_{ridge}^{measured} = A(\omega_n)e^{i\omega_n t} + A'(\omega_n)e^{-i\omega_n t} \qquad 0 < t < T \tag{A.1}$$

Here u and v are the north and east components of the current time series at time t, A and A' are

complex numbers, and $\omega_n = \dfrac{2\pi n}{T}$ represents the set of frequencies where $n = \{0,1,2,\dots N/2\}$

and $N = \dfrac{T}{dt}$. In Equation A.1 and hereafter, a summation on the right hand side over all

constituent frequencies is implied.

23

541   Analogous equations, but in slightly abbreviated form, can be written for the first model

542   input time series at great distance from the ridge (A.2), the first model result at the ridge (A.3),

543   and the second model input times series at great distance from the ridge (A.4):

544

545    $$(u+iv)_{farfield}^{model\,1st} = Be^{i\omega t} + B'e^{-i\omega t} \tag{A.2}$$

546    $$(u+iv)_{ridge}^{model\,1st} = Ce^{i\omega t} + C'e^{-i\omega t} \tag{A.3}$$

547    $$(u+iv)_{farfield}^{model\,2nd} = De^{i\omega t} + D'e^{-i\omega t} \tag{A.4}$$

548

549   In practice, a reasonable choice for B and B' are the amplitudes A and A' of the currents

550   measured at the ridge reduced by a factor of 0.5. An initial model run is made using forcing

551   from Equation A.2. A comparison of the resulting model time series at the ridge (Equation A.3)

552   to the measured current time series at the ridge (Equation A.1) is then used to make a better

553   distant model current time series (Equation A.4).

554   Suppose that the circulation model could be considered a transfer function and suppose

555   that the transfer function were linear. Then the relationship of the time series at the ridge and in

556   the distant ocean (Equations A.2 and A.3) could be written

557    $$(u+iv)_{ridge}^{model\,1st} = \int_0^T M(t-t')(u(t')+iv(t'))_{farfield}^{model\,1st}\,dt' \tag{A.5}$$

558   where M represents the model transform function. Replacing the two current time series in

559   Equation A.5 with their Fourier expansions (Equations A.2 and A.3), we have

560    $$C(\omega_n)e^{i\omega_n t} + C'(\omega_n)e^{-i\omega_n t} = \int_0^T M(t-t')\left(B(\omega_n)e^{i\omega_n t'} + B'(\omega_n)e^{-i\omega_n t'}\right)dt' \tag{A.6}$$

561   Similarly,

24

562 $$A(\omega_n)e^{i\omega_n t} + A'(\omega_n)e^{-i\omega_n t} = \int_0^T M(t-t')\left(D(\omega_n)e^{i\omega_n t'} + D'(\omega_n)e^{-i\omega_n t'}\right)dt' \qquad (A.7)$$

563 By the convolution theorem, Equations A.6 and A.7 yield

564 $$C(\omega_n) = M(\omega_n)B(\omega_n) \qquad \text{and} \qquad A(\omega_n) = M(\omega_n)D(\omega_n) \qquad (A.8)$$

565

566 with like equations for *A', B', C', and D'.*

567 Eliminating $M(\omega_n)$ from Equation pair A.8, as well as from the analogous primed

568 variable equation pair gives:

569 $$D(\omega_n) = \frac{B(\omega_n)A(\omega_n)}{C(\omega_n)} \qquad \text{and} \qquad D'(\omega_n) = \frac{B'(\omega_n)A'(\omega_n)}{C'(\omega_n)} \qquad (A.9)$$

570 Equation A.4 can be re-expressed in the time domain with the Fourier coefficients from A.9

571 $$\left(u + iv\right)_{farfield}^{model\,2nd} = \frac{BA}{C}e^{i\omega t} + \frac{B'A'}{C'}e^{-i\omega t} \quad 0 < t < T \qquad (A.10)$$

572 Resulting in an improved estimate of the far-field forcing time series.

573 The circulation model is in fact not linear and the strong flank currents (Figures 2-4) are

574 partly supported by the nonlinearity of the governing equations. On the other hand, at high

575 frequencies (including tidal frequencies), an assumption of dynamical linearity is often made.

576 Thus, for a substantial part of the frequency spectrum of the measurements, Equation A.10

577 should provide a better estimate than Equation A.2 of the far-field forcing time series.

578 Ultimately it is the correspondence of measured and modeled flow over the ridge crest summed

579 over all frequencies (Figure 1) that provides evidence of the utility of this primitive inverse

580 approach.

581 In principle, there is no need to stop at the second estimate of the distant currents.

582 However, a few pilot experiments we conducted suggested that the benefits of computing a third

583   and fourth estimate were not worth the effort. Results presented herein use the second estimate of

584   far-field currents to force the model. One additional practical matter in evaluating the

585   coefficients of Equation A.9 must be mentioned. Very small values of C and C' at some ω_n lead

586   to unrealistically large spectral coefficients for the second estimate, so that when $|A/C| > 1$ or

587    $|A'/C'| > 1$, the ratio was reset to one. In other words, at each frequency the far-field amplitude

588   must be less than or equal to the amplitude above the ridge.

589   The far-field u,v times-series are used to determine a body force (F_B) or equivalently a

590   horizontal pressure (P_0) gradient that drives the incident barotropic model flow. That force (or

591   pressure gradient) is derived from simple balances that dominate the momentum equation at

592   large distance from the ridge topography, i.e.

593
$$\frac{\partial u}{\partial t} - fv = -\frac{\partial P_0}{\partial x} = F_B^x \qquad \text{and} \qquad \frac{\partial v}{\partial t} + fu = -\frac{\partial P_0}{\partial y} = F_B^y$$

594   where u and v represent the far-field current time series first of Equation A.2 and then of

595   Equation A.4.

References

Adams, D.K. and Mullineaux, L.S., 2008. Supply of gastropod larval to hydrothermal vents reflects transport from local larval sources. Limnology and Oceanography, 53(5): 1945-1955.

Bailly-Bechet, M., Kerszberg, M., Gaill, F. and Pradillon, F., 2008. A modeling approach of the influence of local hydrodynamic conditions on larval dispersal at hydrothermal vents. Journal of Theoretical Biology, 255: 320-331.

Berg, C.J. and Van Dover, C.L., 1987. Benthopelagic macrozooplankton communities at and near deep-sea hydrothermal vents in the eastern Pacific Ocean and the Gulf of California. Deep-Sea Research, 34: 379-401.

Blanton, B., 1995. DROG3D: User's Manual for 3-Dimensional Drogue Tracking on a Finite Element Grid with Linear Finite Elements (see http://www.opnml.unc.edu/Particle_Tracking/part_track.html), Program in Marine Sciences, University of North Carolina, Chapel Hill, NC.

Brink, K.H., 1995. Tidal and lower frequency currents above Fieberling-Guyot. Journal of Geophysical Research, 100: 10,817-10,932.

Cannon, G.A. and Pashinski, D.J., 1997. Variations in mean currents affecting hydrothrmal plumes on the Juan de Fuca Ridge. Journal of Geophysical Research, 102: 24,965-24,976.

Chevaldonné, P., Jollivet, D., Vangriesheim, A. and Desbruyères, D., 1997. Hydrothermal-vent alvinellid polychaete dispersal in the eastern Pacific .1. Influence of vent site distribution, bottom currents, and biological patterns. Limnol Oceanogr 42: 67-80.

Conkright, M.E., Antonov, J.I., Baranova, O., Boyer, T.P., Garcia, H.E., Gelfeld, R., Johnson, D., Locarnini, A., Murphy, P.P., O'Brien, T.D., Smolyar, I. and Stephens, C., 2002. World Ocean Database 2001. NOAA Atlas NESDIS 42, 1: Natl. Oceanic and Atmos. Admin., Silver Spring, Md.

Dittel, A.I. and Epifanio, C.E., 1990. Seasonal and tidal abundances of crab larvae in a tropical mangrove system, Gulf of Nicoya, Costa Rica. Marine Ecology Progress Series, 65: 25-34.

Emery, W.J. and Thomson, R.E., 1998. Data Analysis Methods in Physical Oceanography. Pergamon, New York, 634 pp.

Fornari, D., Haymon, R., Perfit, M., Gregg, T. and Edwards, M., 1998. Axial summit trough of the East Pacific Rice 9°–10°N: Geological characteristics and evolution of the axial zone on fast spreading mid-ocean ridge. Journal of Geophysical Research, 103(B5): 9827-9855.

Forward, R.J., 1988. Diel vertical migration: Zooplankton photobiology and behaviour. Oceanography and Marine Biology: An Annual Review, 26: 361-393.

Garcia Berdeal, I., Hautala, S.L., Thomas, L.N. and Johnson, H.P., 2005. Vertical structure of time-dependent currents in a mid-ocean ridge axial valley. Deep-Sea Research I, 53: 367-386.

Hoegh-Guldberg, O., Welborn, J.R. and Manahan, D.T., 1991. Metabolic requirements of antarctic and temperate asteroid larvae. Antarctic Journal of the United States 26: 163-165.

640   Jackson, G.A. and Strathmann, R.R., 1981. Larval mortality from offshore mixing as a link
641   between precompetent and competent periods of development. American Naturalist, 118:
642   16-26.
643   Jackson, P.R., Ledwell, J.R. and Thurnherr, A.M., in press. Dispersion of a Tracer on the East
644   Pacific Rise (9° N to 10° N), Including the Influence of Hydrothermal Plumes. Deep-Sea
645   Research I.
646   Kim, S.L., Mullineaux, L.S. and Helfrich, K.R., 1994. Larval dispersal via entrainment into
647   hydrothermal vent plumes. Journal of Geophysical Research, 99(C6): 12655-12665.
648   Lavelle, J.W., 1997. Buoyancy-driven plumes in rotating, stratified cross flows: Plume
649   dependence on rotation, turbulent mixing, and cross-flow strength. Journal of
650   Geophysical Research, 102: 3405-342-.
651   Lavelle, J.W., 2006. Flow, hydrography, turbulent mixing, and dissipation at Fieberling Guyot
652   examined with a primitive equation model. Journal of Geophysical Research,
653   111(C07014): doi:10.1029/2005JC003224.
654   Lavelle, J.W. and Thacker, W.C., 2008. A pretty good sponge: Dealing with open boundaries in
655   limited-area ocean models. Ocean Modelling, 20(3): 270-292.
656   Lutz, R.A., Jablonski, D., Rhoads, D.C. and Turner, R.D., 1980. Larval dispersal of a deep-sea
657   hydrothermal vent bivalve from the Galapagos Rift. Marine Biology, 57: 127-133.
658   Marsh, A.G., Mullineaux, L.S., Young, C.M. and Manahan, D.T., 2001. Larval dispersal
659   potential of the tubeworm *Riftia pachyptila* at deep-sea hydrothermal vents. Nature, 411:
660   77-80.
661   Metaxas, A., 2004. Spatial and temporal patterns in larval supply at hydrothermal vents in the
662   northeast Pacific Ocean. Limnology and Oceanography, 49(6): 1949-1956.
663   Mullineaux, L.S., Adams, D.K., Mills, S.W. and Beaulieu, S.E., in preparation. Larval supply
664   and re-colonization of deep-sea hydrothermal vents after a catastrophic eruption.
665   Mullineaux, L.S., Mills, S.W., Sweetman, A.K., Beaudreau, A.H., Metaxas, A. and Hunt, H.L.,
666   2005. Vertical, lateral, and temporal structure in larval distribution at hydrothermal vents.
667   Marine Ecology Progress Series, 293: 1-16.
668   Mullineaux, L.S., Speer, K.G., Thurnherr, A.M., Maltrud, M.E. and Vangriesheim, A., 2002.
669   Implications of cross-axis flow for larval dispersal along mid-ocean ridges. Cahiers de
670   Biologie Marine 43: 281-284.
671   Mullineaux, L.S., Wiebe, P.H. and Baker, E.T., 1995. Larvae of benthic invertebrates in
672   hydrothermal vent plumes over Juan de Fuca Ridge. Marine Biology 122: 585-596.
673   Press, W.H., Flannery, B.P., Teukolsky, S.A. and Vetterling, W.T., 1986. Numerical Recipes.
674   Cambridge University Press, Cambridge.
675   Scheltema, R.S., 1971. The dispersal of larvae of shoalwater benthic invertebrate species over
676   long distances by ocean currents. In: D.J. Crisp (Editor), Fourth European Marine
677   Biology Symposium. Cambridge University Press, Cambridge, pp. 7-28.
678   Smagorinsky, J., 1993. Some historical remarks on the use of nonlinear viscosities. In: B.
679   Galperin and S.A. Orszag (Editors), Large Eddy Simulation of Complex Engineering and
680   Geophysical Flows. Cambridge University Press, pp. 3-36.
681   Smolarkiewicz, P.K. and Margolin, L.G., 1998. MPDATA: A finite-difference solver for
682   geophysical flows. Journal of Computational Physics, 140(2): 459-480.
683   Strathmann, R.R., 1985. Feeding and nonfeeding larval development and life-history evolution in
684   marine invertebrates. Ann. Rev. Ecol. Syst., 16: 339-361.

685   Sulkin, S.D., 1984. Behavioral basis of depth regulation in the larvae of brachyuran crabs.
686   Marine Ecology Progress Series 15: 181-205.
687   Thiebaut, E., Dauvin, J.-C. and Lagadeuc, Y., 1992. Transport of *Owenia fusiformis* larvae
688   (Annelida: Polychaeta) in the Bay of Seine. I. Vertical distribution in relation to water
689   column stratification and ontogenetic vertical migration. Marine Ecological Progress
690   Series 80: 29-39.
691   Thomson, R.E., Mihaly, S.F., Rabinovich, A.B., McDuff, R.E., Scott, R.V. and Stahr, F.R.,
692   2003. Constrained circulation at Endeavour ridge facilitates colonization by vent larvae.
693   Nature, 424: 545-549.
694   Thomson, R.E., Roth, S.E. and Dymond, J., 1990. Near-inertial motions over a mid-ocean ridge:
695   effects of topography and hydrothermal plumes. Journal of Geophysical Research, 95:
696   12,961-12,966.
697   Thurnherr, A.M., Ledwell, J.R. and Lavelle, J.W., in preparation. Regional circulation near the
698   crest of the East Pacific Rise between 9 and 10 N.
699   Tyler, P.A. and Young, C.M., 1999. Reproduction and dispersal at vents and cold seeps. Journal
700   of the Marine Biological Association of the United Kingdom, 79: 193-208.
701   Werner, F.E., Page, F.H., Lynch, D.R., Loder, J.W., Lough, R.G., Perry, R.I., Greenberg, R.M.
702   and Sinclair, M.M., 1993. Influences of mean advection and simple behavior on the
703   distribution of cod and haddock early life stages on Georges Bank. Fisheries
704   Oceanography, 2(2): 43-64.
705   Wilcock, W.S.D., Toomey, D.R., Purdy, G.M. and Solomon, S.C., 1993. The renavigation of Sea
706   Beam bathymetric data between 9° N and 10° N on the East Pacific Rise. Marine
707   Geophysical Researches, 15: 1-12.
708   Young, C.M. and Chia, F.S., 1987. Abundance and distribution of pelagic larvae as influenced
709   by predation, behavior and hydrographic factors. In: A.C. Giese, J.S. Pearse and V.B.
710   Pearse (Editors), Reproduction of Marine Invertebrates, IX, General Aspects: Seeking
711   Unity in Diversity. Blackwell Scientific and The Boxwood Press, Palo Alto and Pacific
712   Grove, CA, pp. 385-463.
713
714

Figure Captions

Figure 1. Simulated and observed currents 175 mab on the EPR ridge crest at 9° 50' N during May – November 1999: (A) zonal (east-west) velocity; (B) meridional (north-south) velocity.

Figure 2. Means and standard deviations of velocities in the zonal (A,D), meridional (B,E), and vertical (C,F) directions simulated for the period May - November, 1999. The black dot indicates the location of the current meter record comparison shown in Figure 1. Time-mean potential density contours for the same time period are superimposed on each panel.

Figure 3. Time series of simulated currents within ±20km of the ridge axis at 2500m (depth of the ridge crest) in the zonal (A), meridional (B), and vertical (C) directions.

Figure 4. Comparison of vertical profiles of time-mean along-ridge velocity simulated at several cross-axis locations in the model with observations from a moored profiler located 10km west of the EPR ridge crest at 9° 30' N. The latter profile consists of means and standard errors for the entire deployment November 2006 – November 2007; standard errors are plotted every eighth data point. Note that variations in vertical extent of the simulated profiles reflect the underlying model bathymetry.

Figure 5. Simulated particle trajectories for a one-month period from September 1, 1999 to October 1, 1999 presented in plan view (A) and vertical cross-section (B). Four sets of particles were released simultaneously at heights of 10 (blue), 125 (green), 175 (black), and 225m (red) above the depth of the ridge crest. Horizontal spacing of the release points was 1km, spanning 20km in the cross-ridge direction. Release locations are indicated by light-blue dots.

Figure 6. Dispersal of particles released every 12 minutes from May to October 1999 at 10, 75, 125, 175, and 225 mab on the ridge crest (release location indicated by white cross). Final positions of each particle at the end of the 30-day larval life span were binned into control volumes with dimensions of 0.44 and 2.5km in the cross- and along-ridge directions respectively. Probability density functions were computed for each of the five depths during six bi-monthly periods: May-June, June-July, July-August, August-September, September-October, and October-November. Particles were released during the first month of each bi-monthly period. The bi-monthly periods overlap in time because the particles released at the end of the first month do not reach the end of the larval life span until the end of the second month. Color shading represents the number of particles residing in each bin, normalized by the total number of particles in each bi-monthly period (3600).

Figure 7. Time series of settlement of numerical larvae, calculated as the fraction of particles with horizontal positions overlying the ridge axis (bin width 0.44km) at the end of the 30-day larval life span.

Figure 8. Time-mean probability density functions for particles with various precompetency periods released every 12 minutes from May to October 1999 at 10, 75, 125, 175, and 225 mab at the ridge crest (release location indicated by white cross). Color shading represents the number of particles residing in 0.44 x 2.5 km bins, normalized by the total number of particles released

761   (108,000). Results for precompetency periods varying from 5 days up to the larval life span (30

762   days) are reported in different rows.

763

764   Figure 9. Dependence of settlement on release depth and precompetency period. Settlement of

765   numerical larvae occurs when their horizontal position is within a grid cell at the ridge crest

766   (width 0.44km) anytime after the precompetency period, but before the end of the larval life

767   span. Shaded contours of settlement are expressed as a percentage of the total particles released.

768

769   Figure 10. Along-axis distribution of particles released every 12 minutes from May to October

770   1999 at 175mab at the ridge crest. These are the same results as presented in the 175mab panel

771   of the top row of Figure 7, plotted as a function of along-axis distance so as to be comparable

772   with Figure 4c of Marsh et al. (2001).

773

	Observed		Modeled	
	u	*v*	*u*	*v*
Mean	-0.29	-0.55	-0.22	0.13
Standard deviation	5.48	3.92	5.8	3.7
RMS difference	*u*: 2.14		*v*: 1.97	
Correlation	*u*: 0.85		*v*: 0.80	

Table 1. Comparison of observed and modeled zonal (*u*) and meridional (*v*) velocities (cm s^{-1}), May–November, 1999. Total number of observations used in the comparison is 4872.

775 **Movies**
776
777 Cross-section release: Simulated particle trajectories for a one-month period from September 1,
778 1999 to October 1, 1999 presented in plan view and in three dimensions. Four sets of passive
779 particles were released at depths of 10, 125, 175, and 225m above the depth of the ridge crest.
780 Horizontal spacing of the release points was 1km, spanning 20km in the cross-ridge direction.
781 Release locations are indicated by light-blue dots.
782
783 http://science.whoi.edu/users/mcgillic/papers/epr2d/movies/cross_section_release/
784
785
786
787 Time-dependent release: Trajectories in the x-y and x-z planes for particles released at 10, 125,
788 175, and 225mab on the ridge crest from September 1-30, 1999. Particles are released at each
789 depth at every time step, so that the total number of particles at each depth is 720. Particles
790 appear as green dots during the thirty days of their larval life span, after which they stop and turn
791 red.
792
793 http://science.whoi.edu/users/mcgillic/papers/epr2d/movies/time_dependent_release/
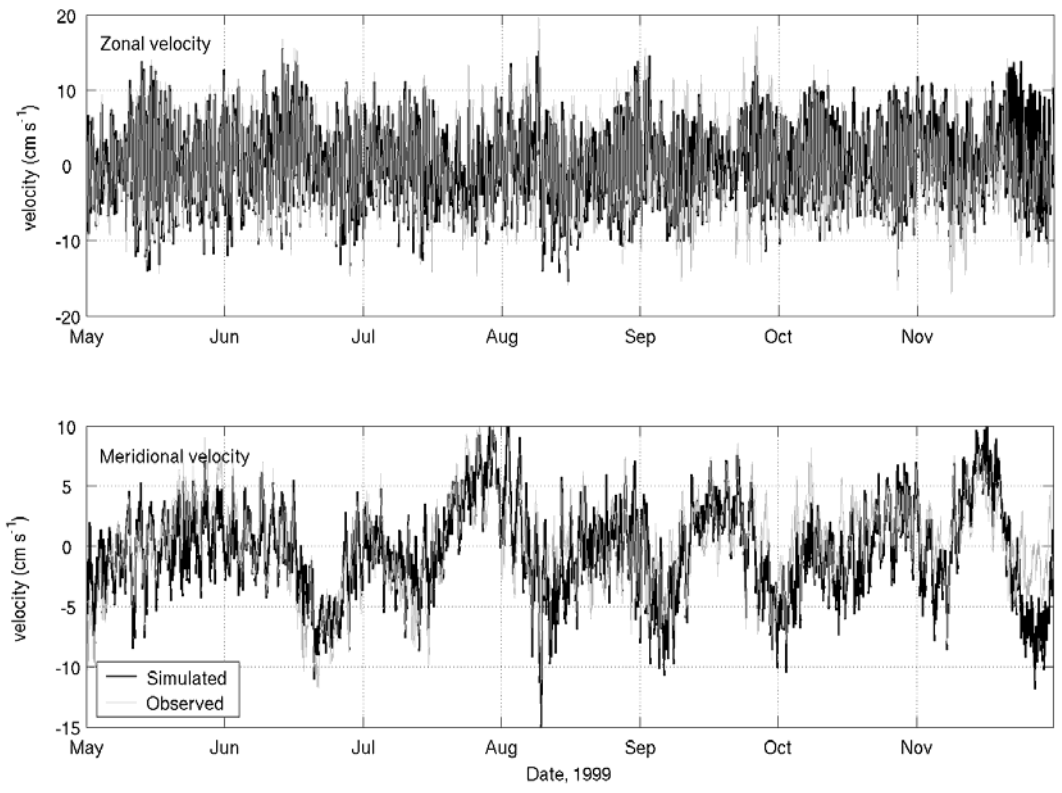
794
795
796
797   McGillicuddy et al., Figure 1.
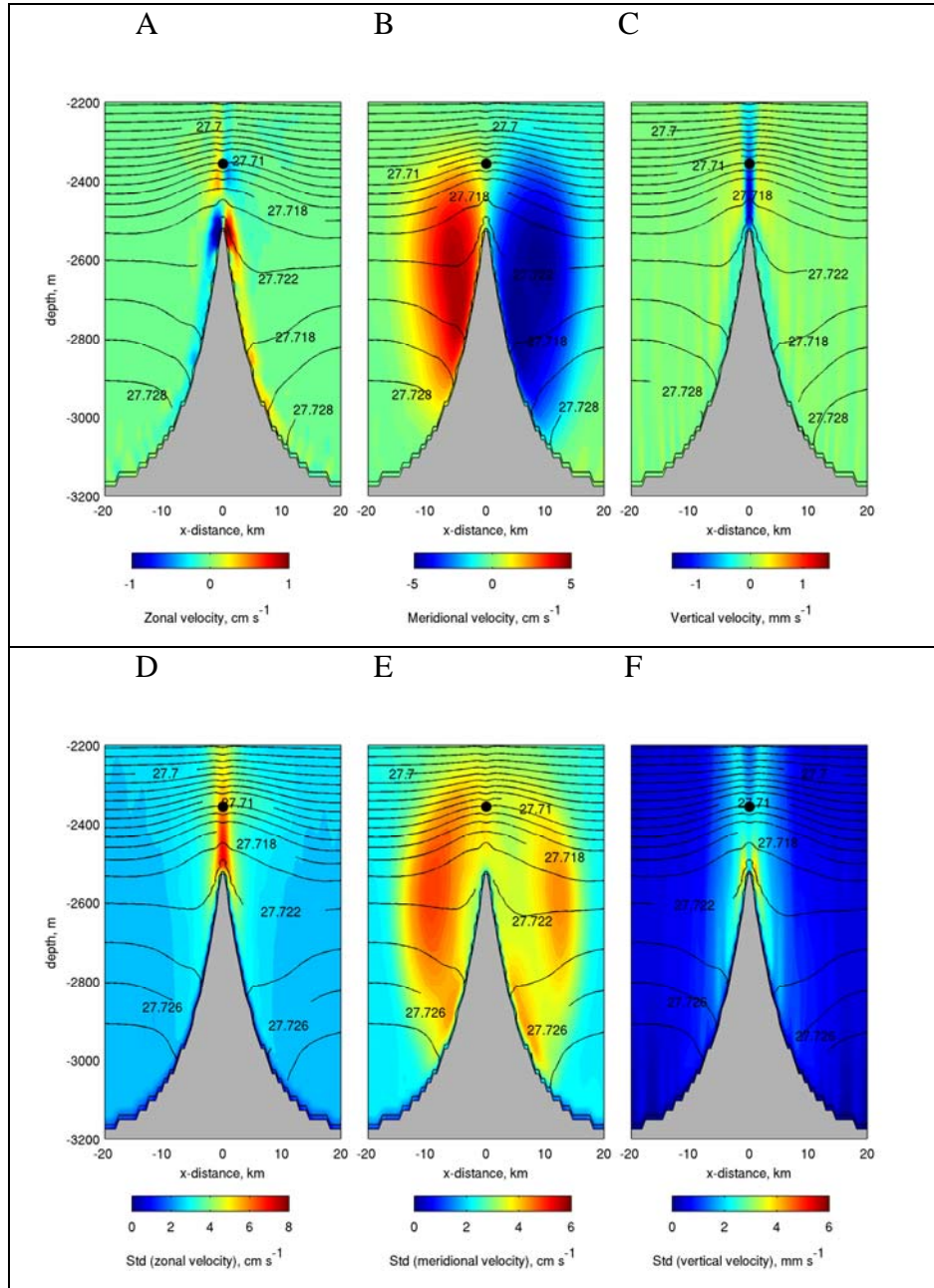
McGillicuddy et al., Figure 2.

804
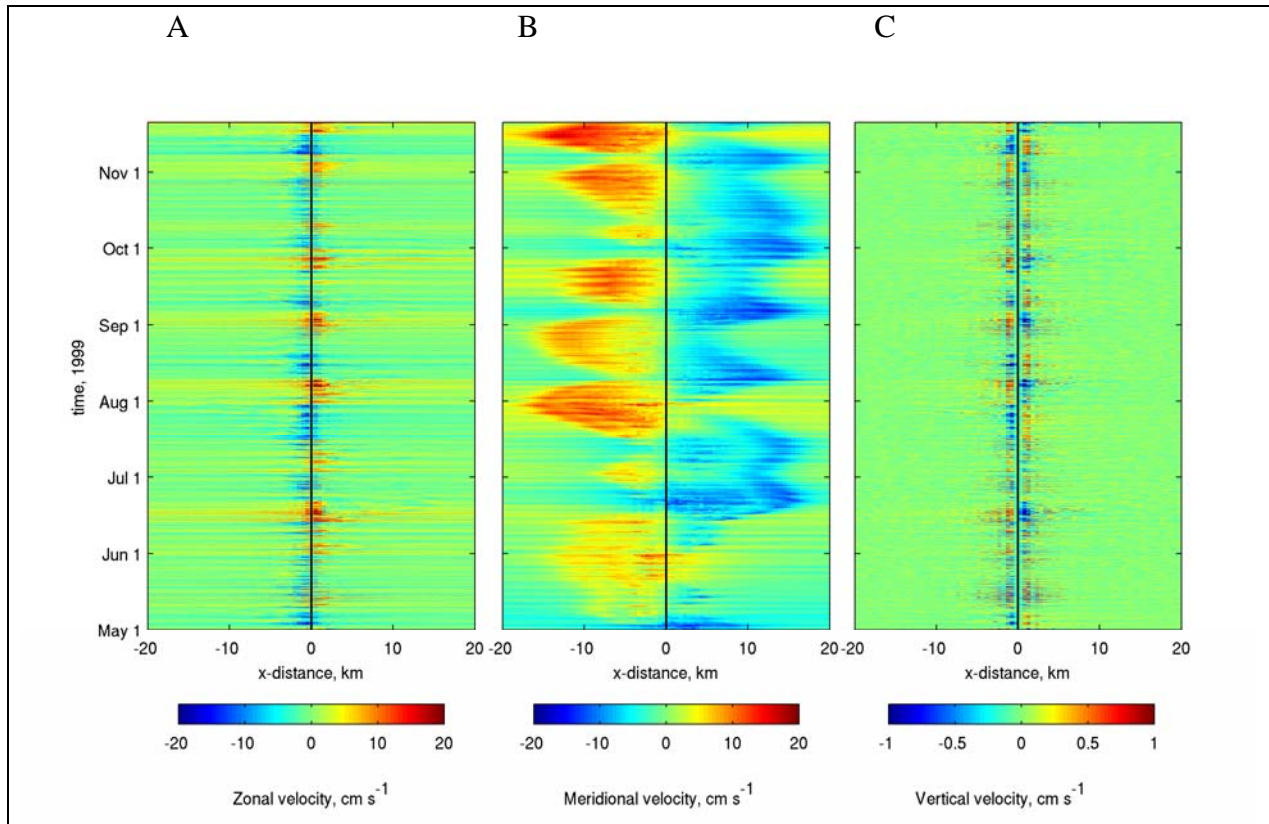
805

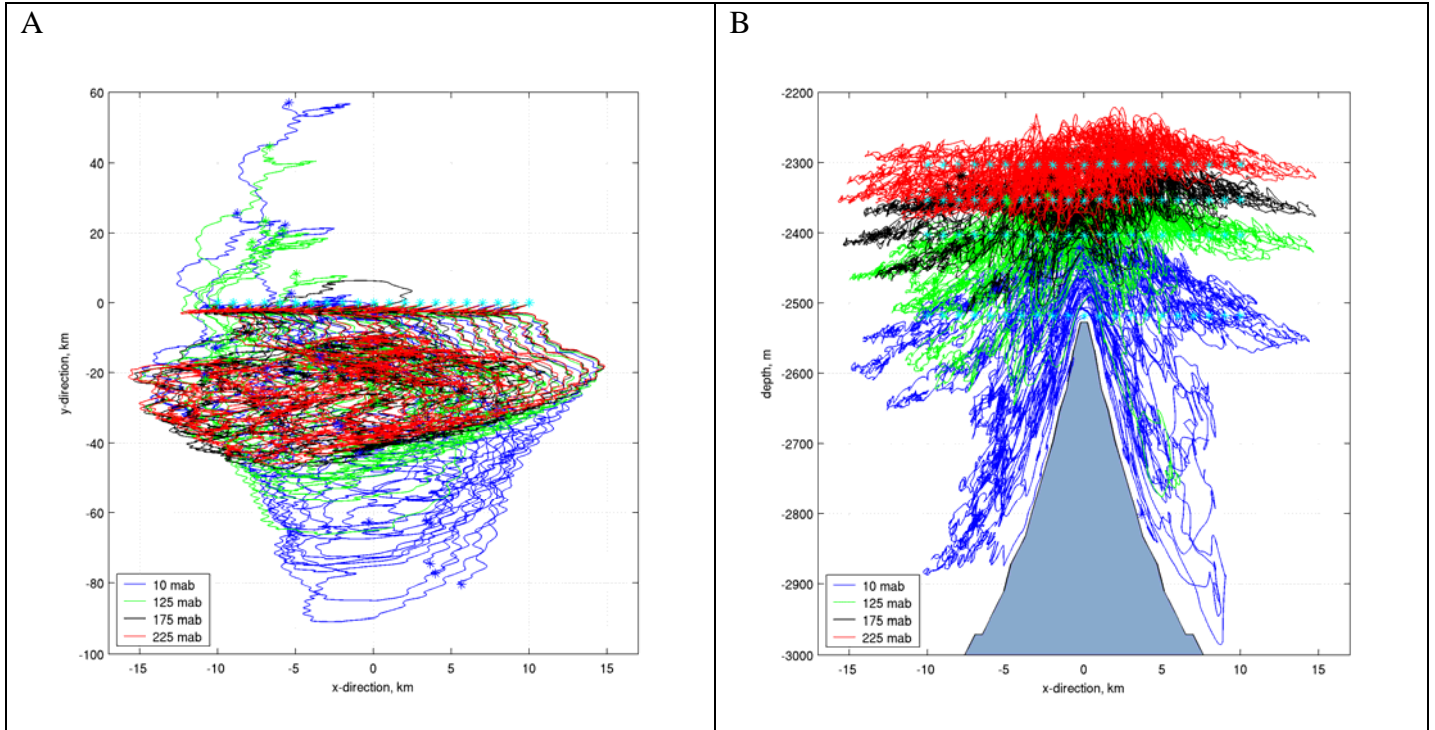806   McGillicuddy et al., Figure 3.
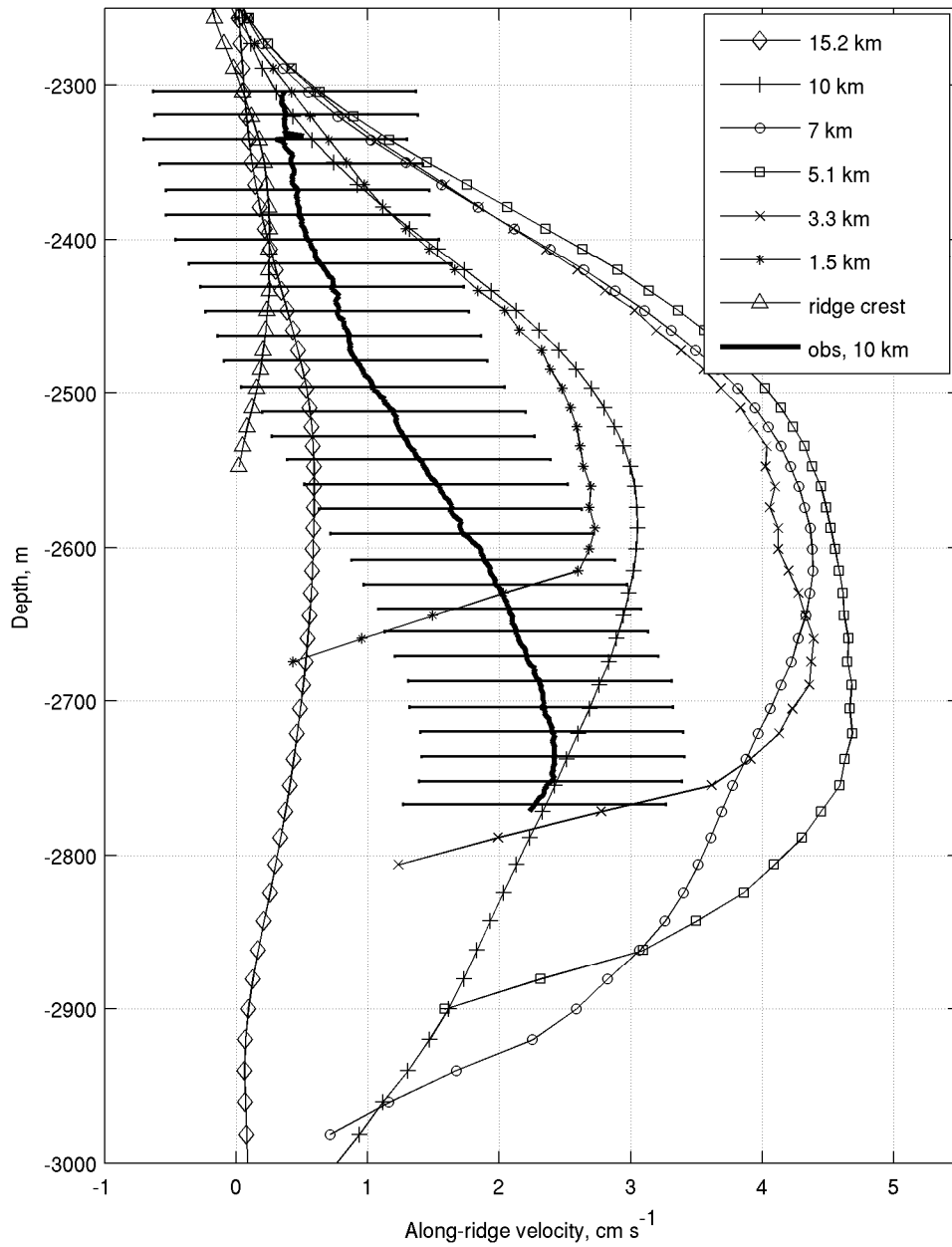
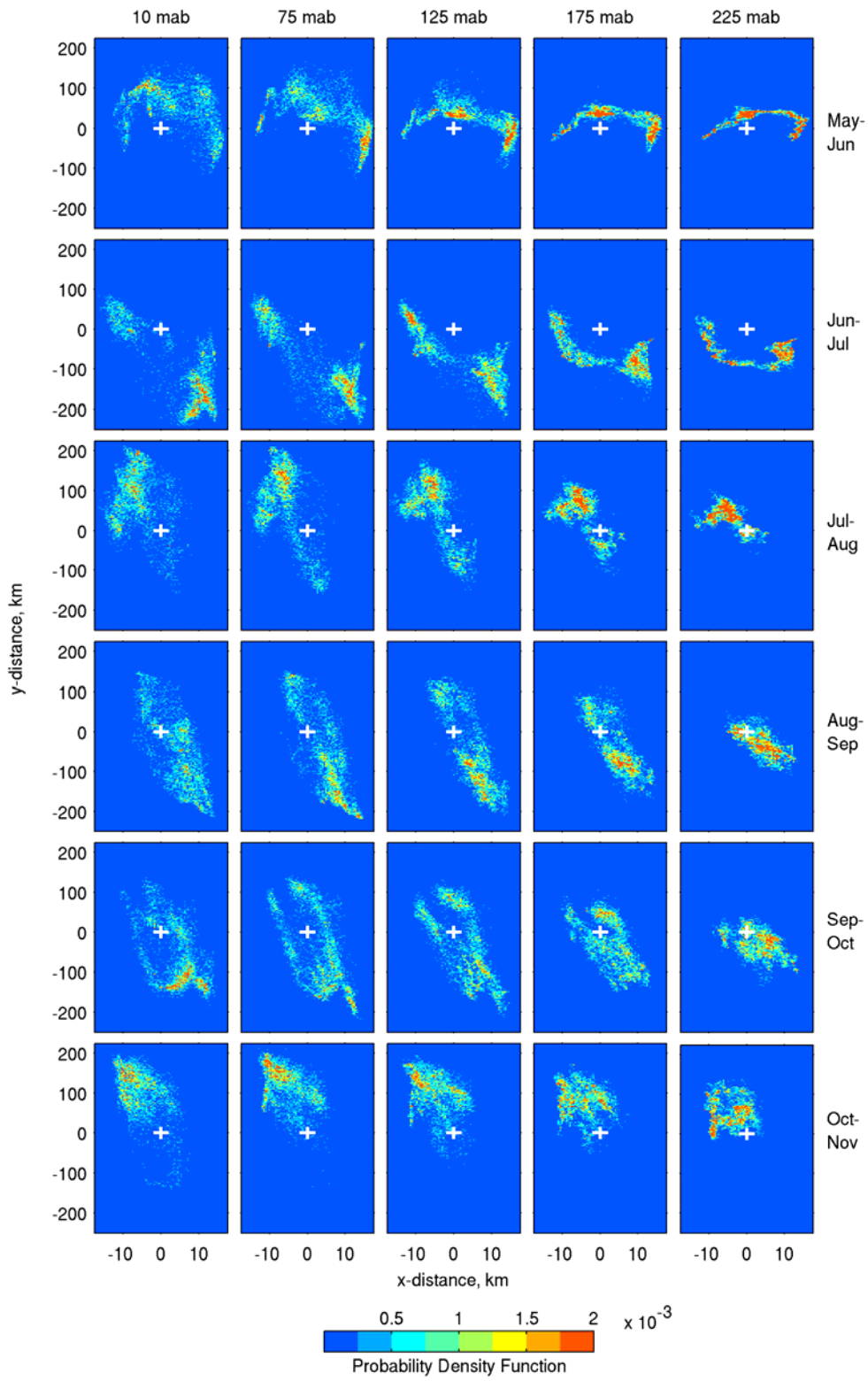McGillicuddy et al., Figure 4.

807
808

809
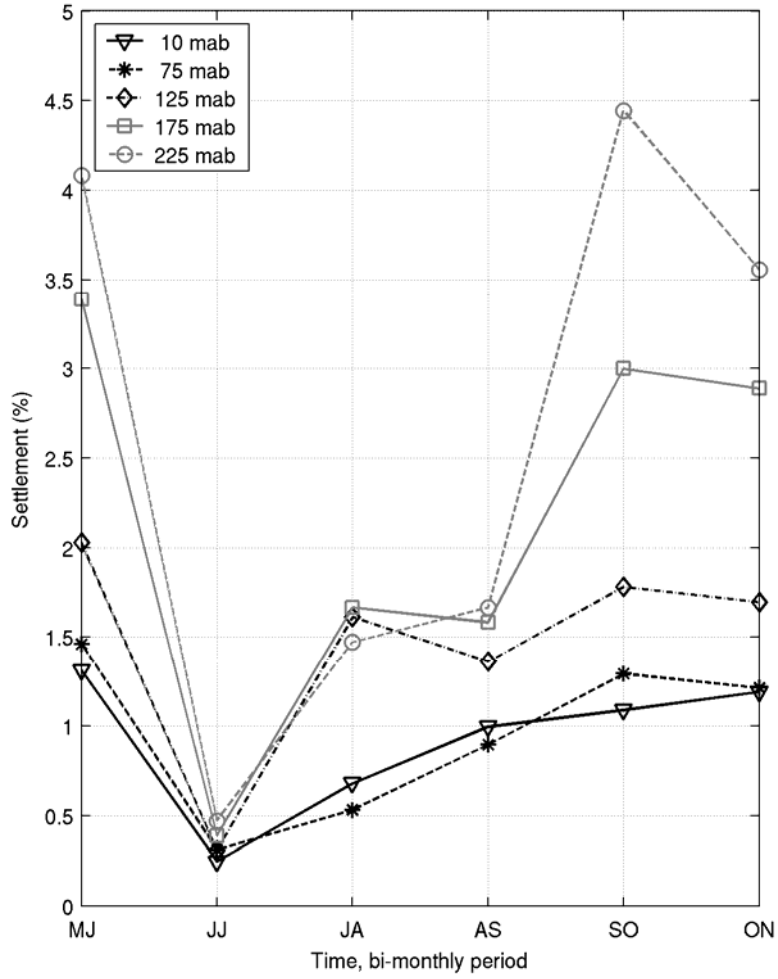810

811
812
813
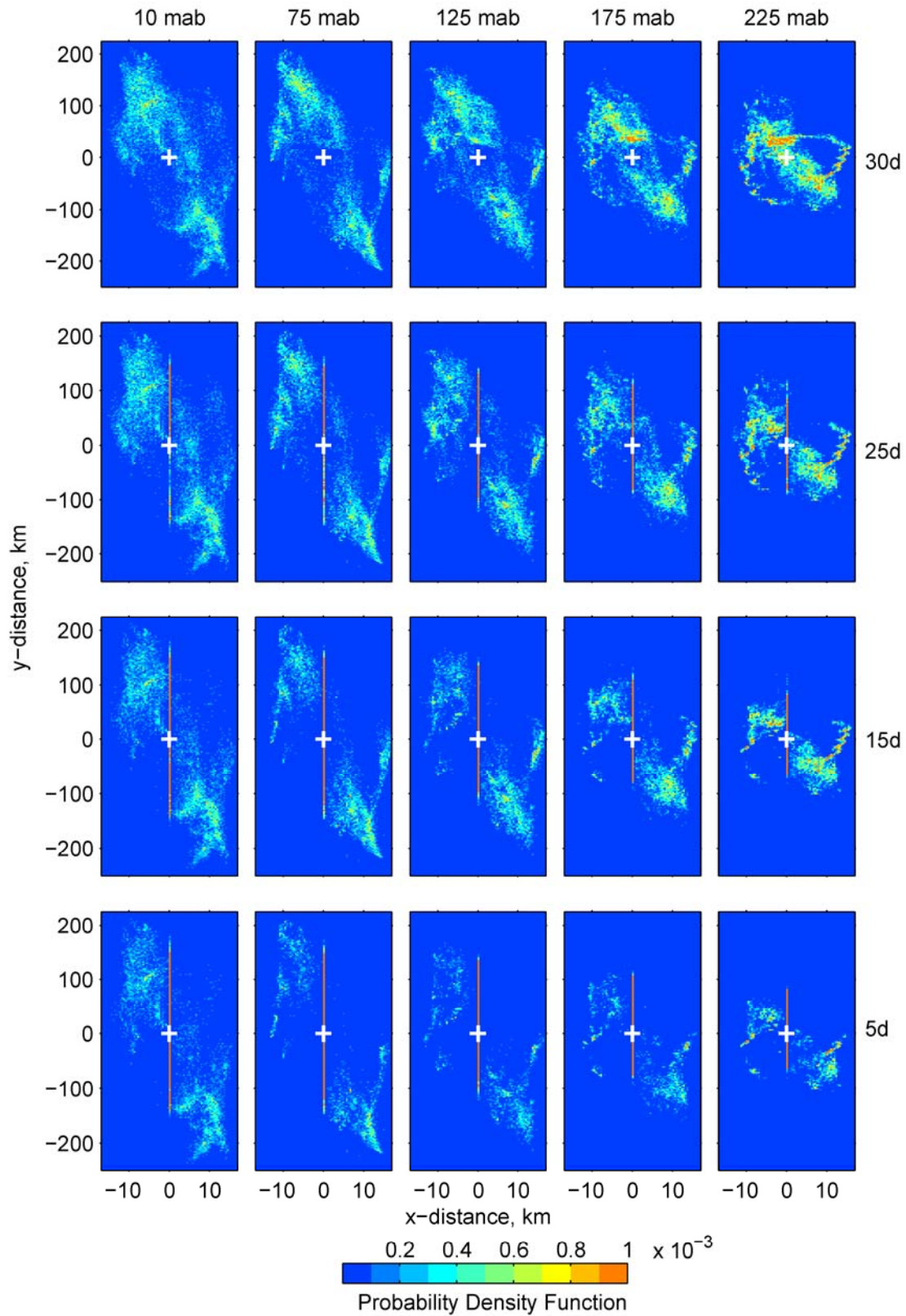814   McGillicuddy et al., Figure 5.

McGillicuddy et al., Figure 6.
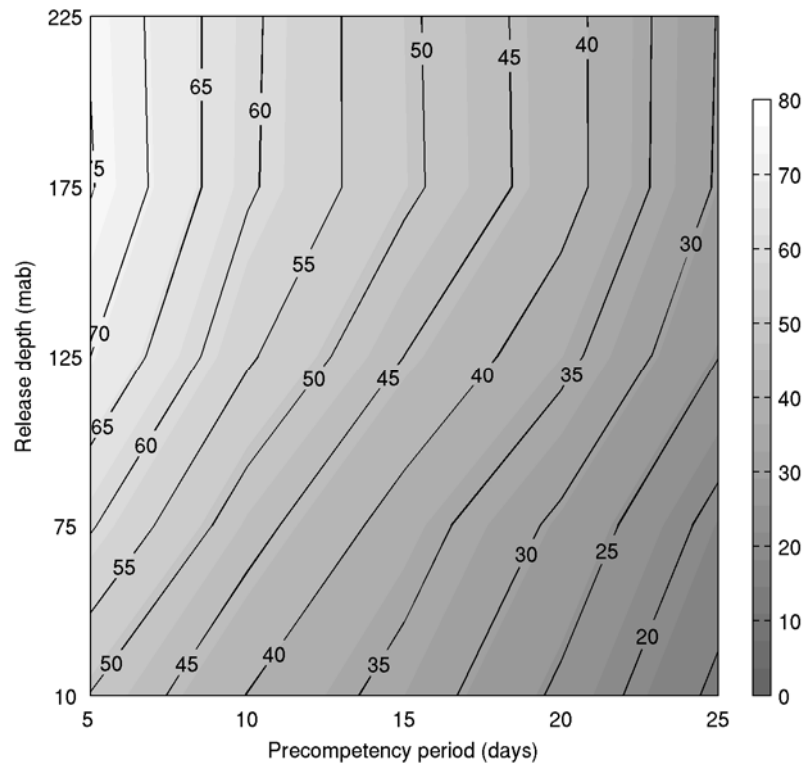
815
816
817
818

819
820
821
822   McGillicuddy et al., Figure 7.
823
824
825
826
827
828
829
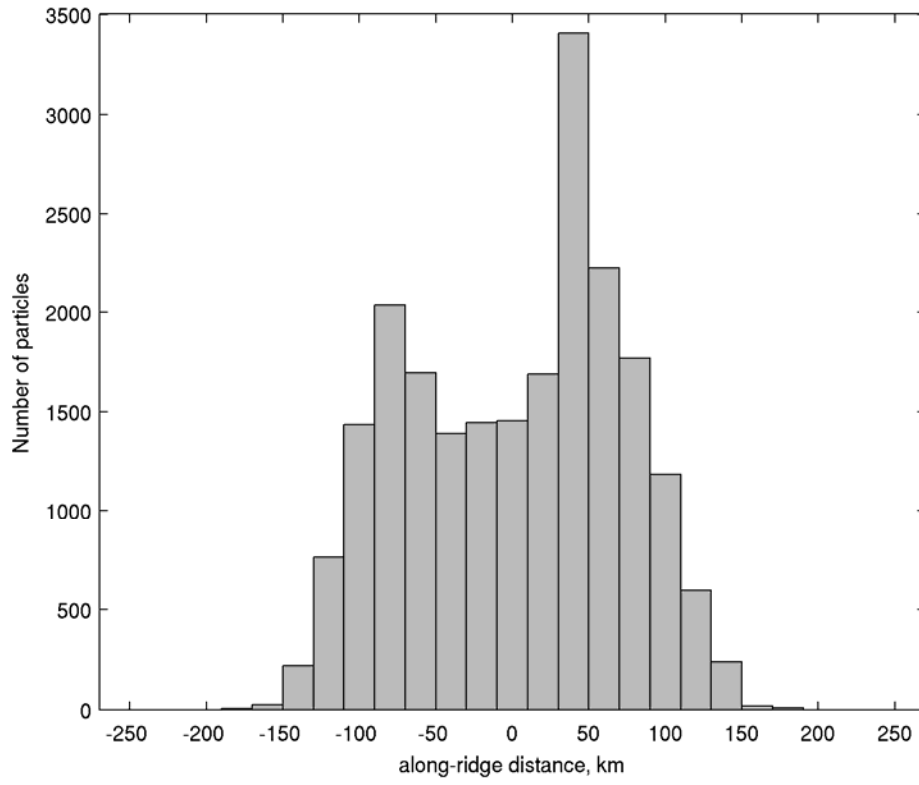830
831
832
833
834
835
836

McGillicuddy et al., Figure 8.

840
841
842
843   McGillicuddy et al., Figure 9.

847   McGillicuddy et al., Figure 10.